

SI for “Bayesian determination of the effect of a deep eutectic solvent on the structure of lipid monolayers”

A. R. McCluskey,^{ab‡} A. Sanchez-Fernandez,^{ac‡¶}

K. J. Edler,^{a*} S. C. Parker,^a A. J. Jackson,^{cd}

R. A. Campbell,^{ef} and T. Arnold^{abcg*}

^a Department of Chemistry, University of Bath, Claverton Down, Bath, BA2 7AY, UK.

^b Diamond Light Source, Harwell Campus, Didcot, OX11 0DE, UK.

^c European Spallation Source, SE-211 00 Lund, Sweden.

^d Department of Physical Chemistry, Lund University, SE-211 00 Lund, Sweden.

^e Institut Laue-Langevin, 71 avenue des Martyrs, 38000, Grenoble, France.

^f Division of Pharmacy and Optometry, University of Manchester, Manchester, M13 9PT, UK.

^g ISIS Neutron and Muon Source, Science and Technology Facilities Council, Rutherford Appleton Laboratory, Harwell Oxford, Didcot OX11 0QX, UK.

¶ Present address: Department of Food Technology, Lund University, SE-211 00 Lund, Sweden.

‡ These authors have contributed equally to the work presented within.

* k.edler@bath.ac.uk; tom.arnold@esss.se

S1 Materials

Choline chloride (99 %, Sigma-Aldrich) and glycerol (99 %, Sigma-Aldrich) d₉-choline chloride (99 %, 98 % D, CK Isotopes) and d₈-glycerol (99 %, 98 % D, CK Isotopes) were purchased and used without further purification. The DES was prepared by mixing the precursors at the appropriate ratio, and heating at 80 °C until a homogeneous, transparent liquid formed.¹ The solvent was equilibrated overnight at 40 °C and subsequently stored under a dry atmosphere. Due to the limited availability of the deuterated precursors, a fully protonated subphase (hDES) and a partially deuterated

subphase (hdDES) were prepared and used during the neutron reflectometry (NR) experiment. The partially deuterated subphase was prepared using the following mixtures of precursors: 1 mol of 0.38 mole-fraction of h-choline chloride/0.62 mole-fraction of d-choline chloride; and 2 mol of 0.56 mole-fraction of h-glycerol/0.44 mole-fraction of d-glycerol. The solvent was subsequently prepared following the procedure discussed above.

The water content of the DES was determined before and after each experiment by Karl-Fischer titration (Mettler Toledo DL32 Karl-Fischer Coulometer, Aqualine Electrolyte A, Aqualine Catholyte CG A) in order to ensure water presence was kept to a minimum. Those measurements showed that the water content of the solvent was kept below 0.3 wt% during all the experimental procedures presented here, which we assume to be negligible and have little impact on the characteristics of the DES.^{2,3}

DPPC (>99 %, C₁₆ tails), DMPC (>99 %, C₁₄ tails), and DMPG (>99 %, C₁₄ tails) were supplied by Avanti Polar Lipids and DLPC (>99 %, C₁₂ tails) was supplied by Sigma-Aldrich and all were used as received. Deuterated versions of DPPC (d₆₂-DPPC, >99 %, deuterated tails-only) and DMPC (d₅₄-DPPC, >99 %, deuterated tails-only) were supplied by Avanti Polar Lipids and used without further purification. These phospholipids were dissolved in chloroform (0.5 mg mL⁻¹) at room temperature. PC indicates the molecule contains a phosphocholine head component, where PG contains a phosphoditylglycerol head component, these are shown in Figure 1.

In the XRR experiment, sample preparation was performed *in situ* using the standard method for the spreading of insoluble monolayers on water: a certain amount of the phospholipid solution was spread onto the liquid surface in order to provide a given surface concentration. After the evaporation of the chloroform, it is assumed that the resulting system is a solvent subphase with a monolayer of phospholipid at the interface. Surface concentration was modified by closing and opening the PTFE barriers of a Langmuir trough. In order to minimise the volumes used in the NR experiment (to keep the cost of deuterated compounds to a manageable level) it was not possible to use a Langmuir trough. Instead, small Delrin adsorption troughs were used that did not have controllable barriers. So, although the surface coverage was nominally the same as used in the X-ray studies, the lack of precise control over the surface pressure meant that it was not appropriate to co-refine XRR and NR contrasts together.

S2 Methods

XRR measurements were taken on I07 at Diamond Light Source, at 12.5 keV photon energy using the double-crystal-deflector.⁴ The reflected intensity was measured in a momentum transfer range from 0.018 Å⁻¹ to 0.7 Å⁻¹. The data were normalised with respect to the incident beam and the back-

ground was measured from off-specular reflection and subsequently subtracted. Samples were equilibrated for at least one hour and preserved under an argon atmosphere to minimise the adsorption of water by the subphase. XRR data were collected for each of the lipids, DLPC, DMPC, DPPC and DMPG at four surface pressures (DLPC: 20, 25, 30, and 35 mNm⁻¹, DMPC: 20, 25, 30, and 40 mNm⁻¹, DPPC: 15, 20, 25, and 30 mNm⁻¹, DMPG: 15, 20, 25, and 30 mNm⁻¹), as measured with an aluminium Wilhelmy plate; all measurements were conducted at 22 °C. The aluminium Wilhelmy plate was used over a traditional paper plate due to the low wettability of paper by the DES.

The NR experiments were performed on FIGARO at the Institut Laue-Langevin using the time-of-flight method.⁵ Data at two incident angles of 0.62° and 3.8° were measured to provide a momentum transfer range from 0.005 Å⁻¹ to 0.18 Å⁻¹. Two surface pressures for each system and contrast was measured (DMPC: 20 and 25 mNm⁻¹, DPPC: 15 and 20 mNm⁻¹). Similar to the X-ray procedure, samples were given enough time to equilibrate (at least two hours), kept under an inert atmosphere, and all measurements were conducted at 22 °C.

S3 Literature values for head and tail volumes

Table SI gives a variety of literature values for the component volumes of the lipids investigated in this work.

S4 Chemically-consistant model

Our chemically-consistent model is made up of two layers to define the lipid monolayer; the head layer at the interface with the solvent and tail layer at the interface with the air. The head components have a calculated scattering length, b_h , (found as a summation of the X-ray or neutron atomic scattering lengths), and a component volume, V_h . These head components make up a layer with a given thickness, d_h , and roughness, σ_h , within which some volume fraction of solvent can intercalate, ϕ_h . The tail components also have a calculated scattering length, b_t , roughness, σ_t , and a component volume, V_t . We have defined the thickness of the tail layer, d_t , in terms of the maximum (all-trans) length of the carbon tail, t_t , and the angle that the chain is tilted by with respect to the interface normal, θ_t ,

$$d_t = t_t \cos \theta_t. \quad (\text{S1})$$

This was used to impose a chemically-sensible maximum on the thickness of the lipid tail layer, e.g. it cannot be thicker than the maximum extended length of the lipid tail. The scattering length density (SLD) of the tail and

Table SI: Lipid component volumes extracted from different literature sources. V_l corresponds to the total lipid volume, MD to molecular dynamics simulation, WAXS to wide-angle X-ray scattering, NB to neutral buoyancy and DVTD to differential vibrating tube densimetry. ^a The values for the head component in Kucerka *et al.*,⁶ were taken from Balgavý *et al.*⁷

Lipid	DPPC	DMPC	DLPC	DMPG	POPG
Reference	[8]	[9]	[8]	[8]	[11]
$V_l/\text{\AA}^3$	1287.3 ± 25.5	1148 ± 2	1264.2 ± 32.1	1172.5 ± 25.1	1155.4 ± 30.0
$V_t/\text{\AA}^3$	966.4 ± 5.4	829 ± 4	924.7 ± 17.6	851.5 ± 5.0	815.9 ± 15.5
$V_h/\text{\AA}^3$	320.9 ± 20.1	319 ± 6	339.5 ± 14.5	320.9 ± 20.1	339.5 ± 14.5
Method	MD	WAXS	NB	MD	NB
T/°C	50	24	30	50	30

head layers used in the Abelès model can therefore be found as follows,

$$\text{SLD}_i = \frac{b_i}{V_i} (1 - \phi_i) + \text{SLD}_s(\phi_i), \quad (\text{S2})$$

where, SLD_s is the scattering length density of the subphase (DES), and i indicates either the tail or head layer; it is assumed that the tail layer contains neither solvent nor air, e.g. $\phi_t = 0$. To ensure that the number density of head components and pairs of tail components is the same, the following constraint was included in the model,¹²

$$\phi_h = 1 - \left(\frac{d_t V_h}{V_t d_h} \right). \quad (\text{S3})$$

Based on the work of Campbell *et al.*,¹³ a single value for the interfacial roughness was fitted for all of the interfaces, including the subphase (i.e. $\sigma_h = \sigma_t = \sigma_s$), as there is only a single lipid molecule type in each monolayer. Therefore, any capillary wave roughness at the air-DES interface is carried equally through the layers.

Table SII: The invariant parameters within the chemically-consistent model. ^aValues obtained from the Tanford formula.¹⁴ ^bValues obtained from Sanchez-Fernandez *et al.*¹⁵

Component	b_t/fm	b_h/fm	$t_t/\text{\AA}$	$\text{SLD}/\times 10^{-6}\text{\AA}^{-2}$
X-ray				
DLPC	5073	4674	15.5 ^a	–
DMPC	5985	4674	18.0 ^a	–
DPPC	6897	4674	20.5 ^a	–
DMPG	5985	4731	18.0 ^a	–
Air	–	–	–	0
DES	–	–	–	10.8 ^b
Neutron				
d ₅₄ -DMPC	5329.8	602.7	18.0 ^a	–
d ₆₂ -DPPC	6129.2	602.7	20.5 ^a	–
h-DES	–	–	–	0.43 ^b
hd-DES	–	–	–	3.15 ^b

S5 XRR parameters at each surface pressure

Tables SIII-SV gives the best fit values for the custom model that was fitted to each surface pressure, for each lipid. These values were used for comparison to assess the effect of the choline chloride:glycerol on the lipid.

Table SIII: The best-fit values, and associated 95 % confidence intervals for the varying parameters in the XRR models, at the second highest surface pressure (SP) measured. The values of d_t were found from the values of θ_t using Eqn. S1 and the values for ϕ_h were obtained from the use of Eqn. S3

Lipid SP/mNm ⁻¹	DLPC 30	DMPC 30	DPPC 25	DMPG 25
$\theta_t/^\circ$	$51.99^{+0.18}_{-0.19}$	$40.28^{+0.06}_{-0.06}$	$34.89^{+0.07}_{-0.06}$	$47.13^{+0.05}_{-0.04}$
$\sigma_{t,h,s}/\text{\AA}$	$4.16^{+0.03}_{-0.02}$	$3.86^{+0.00}_{-0.00}$	$4.31^{+0.00}_{-0.00}$	$3.81^{+0.00}_{-0.00}$
$V_t/\text{\AA}^3$	$625.21^{+3.70}_{-4.06}$	$718.75^{+0.55}_{-0.53}$	$765.32^{+0.40}_{-0.37}$	$733.99^{+0.60}_{-0.60}$
$V_h/\text{\AA}^3$	$331.43^{+0.64}_{-0.64}$	$339.55^{+0.29}_{-0.28}$	$322.00^{+0.24}_{-0.25}$	$329.94^{+0.34}_{-0.33}$
$d_h/\text{\AA}$	$10.99^{+0.13}_{-0.14}$	$13.21^{+0.04}_{-0.04}$	$12.70^{+0.03}_{-0.03}$	$13.95^{+0.03}_{-0.03}$
$\phi_h/\times 10^{-2}$	$54.12^{+1.08}_{-1.12}$	$50.93^{+0.24}_{-0.23}$	$44.24^{+0.23}_{-0.21}$	$60.57^{+0.17}_{-0.17}$
$d_t/\text{\AA}$	$9.52^{+0.04}_{-0.04}$	$13.72^{+0.01}_{-0.01}$	$16.83^{+0.01}_{-0.01}$	$12.24^{+0.01}_{-0.01}$

Table SIV: The best-fit values, and associated 95 % confidence intervals for the varying parameters in the XRR models, at the second lowest surface pressure (SP) measured. The values of d_t were found from the values of θ_t using Eqn. S1 and the values for ϕ_h were obtained from the use of Eqn. S3

Lipid SP/mNm ⁻¹	DLPC 25	DMPC 25	DPPC 20	DMPG 20
$\theta_t/^\circ$	$57.53^{+0.17}_{-0.17}$	$47.63^{+0.05}_{-0.05}$	$36.11^{+0.07}_{-0.06}$	$53.73^{+0.04}_{-0.04}$
$\sigma_{t,h,s}/\text{\AA}$	$4.36^{+0.02}_{-0.02}$	$3.92^{+0.01}_{-0.01}$	$4.09^{+0.00}_{-0.00}$	$3.94^{+0.01}_{-0.01}$
$V_t/\text{\AA}^3$	$625.21^{+3.70}_{-4.06}$	$718.75^{+0.55}_{-0.53}$	$765.32^{+0.40}_{-0.37}$	$733.99^{+0.60}_{-0.60}$
$V_h/\text{\AA}^3$	$331.43^{+0.64}_{-0.64}$	$339.55^{+0.29}_{-0.28}$	$322.00^{+0.24}_{-0.25}$	$329.94^{+0.34}_{-0.33}$
$d_h/\text{\AA}$	$10.99^{+0.13}_{-0.14}$	$13.21^{+0.04}_{-0.04}$	$12.70^{+0.03}_{-0.03}$	$13.95^{+0.03}_{-0.03}$
$\phi_h/\times 10^{-2}$	$60.00^{+0.94}_{-0.98}$	$56.66^{+0.21}_{-0.20}$	$45.08^{+0.23}_{-0.21}$	$65.72^{+0.14}_{-0.14}$
$d_t/\text{\AA}$	$8.30^{+0.04}_{-0.04}$	$12.12^{+0.01}_{-0.01}$	$16.57^{+0.01}_{-0.01}$	$10.64^{+0.01}_{-0.01}$

Table SV: The best-fit values, and associated 95 % confidence intervals for the varying parameters in the XRR models, at the lowest surface pressure (SP) measured. The values of d_t were found from the values of θ_t using Eqn. S1 and the values for ϕ_h were obtained from the use of Eqn. S3

Lipid SP/mNm ⁻¹	DLPC 20	DMPC 20	DPPC 15	DMPG 15
$\theta_t/^\circ$	$63.26^{+0.13}_{-0.12}$	$58.51^{+0.04}_{-0.05}$	$38.98^{+0.06}_{-0.06}$	$71.50^{+0.18}_{-0.18}$
$\sigma_{t,h,s}/\text{\AA}$	$4.23^{+0.02}_{-0.02}$	$4.20^{+0.01}_{-0.01}$	$3.88^{+0.00}_{-0.00}$	$4.65^{+0.01}_{-0.01}$
$V_t/\text{\AA}^3$	$625.21^{+3.70}_{-4.06}$	$718.75^{+0.55}_{-0.53}$	$765.32^{+0.40}_{-0.37}$	$733.99^{+0.60}_{-0.60}$
$V_h/\text{\AA}^3$	$331.43^{+0.64}_{-0.64}$	$339.55^{+0.29}_{-0.28}$	$322.00^{+0.24}_{-0.25}$	$329.94^{+0.34}_{-0.33}$
$d_h/\text{\AA}$	$10.99^{+0.13}_{-0.14}$	$13.21^{+0.04}_{-0.04}$	$12.70^{+0.03}_{-0.03}$	$13.95^{+0.03}_{-0.03}$
$\phi_h/\times 10^{-2}$	$66.48^{+0.76}_{-0.78}$	$66.41^{+0.16}_{-0.16}$	$47.15^{+0.22}_{-0.21}$	$81.62^{+0.18}_{-0.17}$
$d_t/\text{\AA}$	$6.95^{+0.03}_{-0.03}$	$9.39^{+0.01}_{-0.01}$	$15.95^{+0.01}_{-0.01}$	$5.71^{+0.05}_{-0.05}$

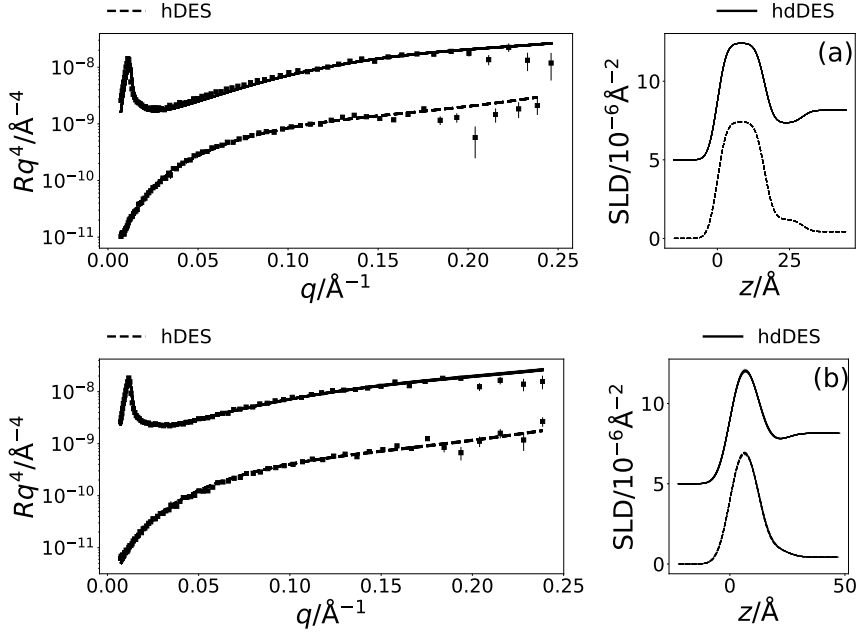


Figure S1: The NR and SLD profiles at a surface pressure of (a) 25 mNm⁻¹ for two contrasts of DMPC, and (b) 15 mNm⁻¹ for two contrasts of DPPC. The NR profiles have been offset in the y -axis by an order of magnitude and SLD profiles offset in the y -axis by $5 \times 10^{-6} \text{\AA}^{-2}$, for clarity.

S6 Neutron reflectometry and SLD profiles

Figure S1 shows the neutron reflectometry and scattering length density profiles for DMPC at 25 mN m⁻¹ (two contrasts) and DPPC at 15 mN m⁻¹ (two contrasts).

S7 Grazing incident X-ray diffraction (GIXD)

GIXD was measured for DPPC and DMPC at 30 mN m⁻¹ at 22 °C (and 7 °C for DMPC), and are shown in Figures S2-S4. All figures contain an artifact from the X-ray beam interacting with the Teflon of the Langmuir trough. However, in figures S2 and S4 it is possible to identify a (2, 0) diffraction peak that indicates the presence of a similar structure to that found under the same conditions in water.¹⁶ Based on this information we believe that, similar to water, the phase of the lipid tails is likely to be in the liquid phase at all surface pressures measured.

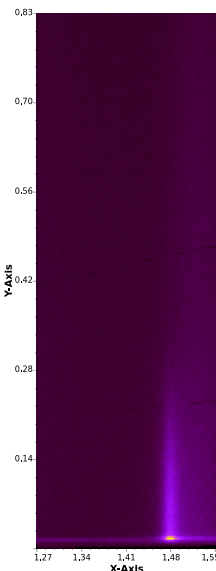


Figure S2: The GIXD pattern for DPPC at 30 mN m^{-1} at $22\text{ }^\circ\text{C}$, the axes at in units of \AA^{-1} . Source: Datasets, figure files and running/plotting scripts are available under CC-BY.¹⁷

S8 Probability distribution functions

The two-dimensional probability distribution functions (PDFs) for all parameters and all lipids from the X-ray reflectometry models are given in Figures S5-S20. The two-dimensional probability distribution functions (PDFs) for all parameters and all lipids from the neutron reflectometry models are given in Figures S21-S24.

References

- [1] E. L. Smith, A. P. Abbott and K. S. Ryder, *Chem. Rev.*, 2014, **114**, 11060–11082.
- [2] O. S. Hammond, D. T. Bowron and K. J. Edler, *Green Chem.*, 2016, **18**, 2736–2744.
- [3] O. S. Hammond, D. T. Bowron, A. J. Jackson, T. Arnold, A. Sanchez-Fernandez, N. Tsapataris, V. G. Sakai and K. J. Edler, *J. Phys. Chem. B*, 2017, **121**, 7473–7483.

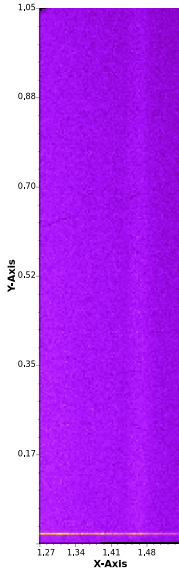


Figure S3: The GIXD pattern for DMPC at 30 mN m^{-1} at $22\text{ }^\circ\text{C}$, the axes at in units of \AA^{-1} . Source: Datasets, figure files and running/plotting scripts are available under CC-BY.¹⁷

- [4] T. Arnold, C. Nicklin, J. Rawle, J. Sutter, T. Bates, B. Nutter, G. McIn tyre and M. Burt, *J. Synchrotron Rad.*, 2012, **19**, 408–416.
- [5] R. A. Campbell, H. P. Wacklin, I. Sutton, R. Cubitt and G. Fragneto, *Eur. Phys. J. Plus*, 2011, **126**, 107.
- [6] N. Kučerka, M. A. Kiselev and P. Balgavý, *Eur. Biophys. J.*, 2004, **33**, 328–334.
- [7] P. Balgavý, N. Kučerka, V. I. Gordeliy and V. G. Cherezov, *Acta Phys. Solvaca*, 2001, **51**, 53–68.
- [8] R. S. Armen, O. D. Uitto and S. E. Feller, *Biophys. J.*, 1998, **75**, 734–744.
- [9] W. J. Sun, R. M. Suter, M. A. Knewton, C. R. Worthington, S. Tristram-Nagle, R. Zhang and J. F. Nagle, *Phys. Rev. E*, 1994, **49**, 4665–4676.
- [10] J. Pan, F. A. Heberle, S. Tristram-Nagle, M. Szymanski, M. Koepfinger, J. Katsaras and N. Kučerka, *BBA - Biomembranes*, 2012, **1818**, 2135–2148.

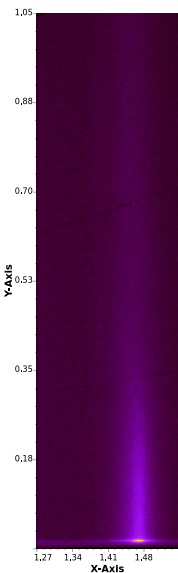


Figure S4: The GIXD pattern for DMPC at 30 mN m^{-1} at 7°C , the axes at in units of \AA^{-1} . Source: Datasets, figure files and running/plotting scripts are available under CC-BY.¹⁷

- [11] N. Kučerka, B. W. Holland, C. G. Gray, B. Tomberli and J. Katsaras, *J. Phys. Chem. B*, 2012, **116**, 232–232.
- [12] L. Braun, M. Uhlig, R. von Klitzing and R. A. Campbell, *Adv. Colloid Interface Sci*, 2017, **247**, 130–148.
- [13] R. A. Campbell, Y. Saaka, Y. Shao, Y. Gerelli, R. Cubitt, E. Nazaruk, D. Matyszewska and M. J. Lawrence, *J. Colloid Interface Sci.*, 2018, **531**, 98–108.
- [14] C. Tanford, *The Hydrophobic Effect: Formation of Micelles and Biological Membranes*, John Wiley & Sons Ltd., Somerset, NJ, USA, 2nd edn, 1980.
- [15] A. Sanchez-Fernandez, T. Arnold, A. J. Jackson, S. L. Fussell, R. K. Heenan, R. A. Campbell and K. J. Edler, *Phys. Chem. Chem. Phys.*, 2016, **18**, 33240–33249.
- [16] E. B. Watkins, C. E. Miller, D. J. Mulder, T. L. Kuhl, and J. Majewski, *Phys. Rev. Lett.*, 2009, **102**, 238101.

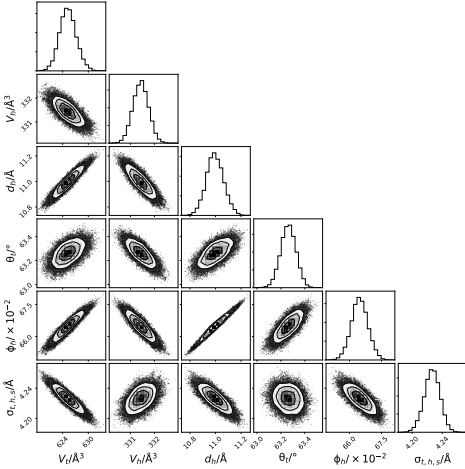


Figure S5: The multi-parameter PDFs for the chemically-relevant model of DLPC X-ray reflectometry data at 20 mNm^{-1} . Source: Datasets, figure files and running/plotting scripts are available under CC-BY.¹⁷

- [17] A. R. McCluskey, *XRR, and SLD profiles, head volume PDFs and tail thickness and solvent fraction. Data, figures and plotting script on figshare*, 2018, <https://doi.org/10.6084/m9.figshare.7053410>.

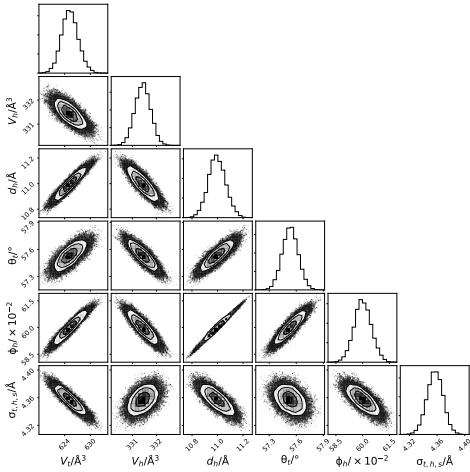


Figure S6: The multi-parameter PDFs for the chemically-relevant model of DLPC X-ray reflectometry data at 25 mNm^{-1} . Source: Datasets, figure files and running/plotting scripts are available under CC-BY.¹⁷

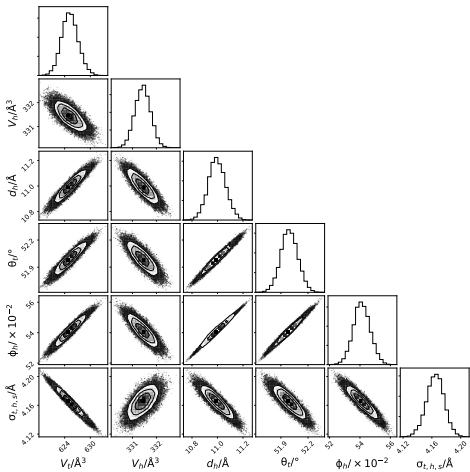


Figure S7: The multi-parameter PDFs for the chemically-relevant model of DLPC X-ray reflectometry data at 30 mNm^{-1} . Source: Datasets, figure files and running/plotting scripts are available under CC-BY.¹⁷

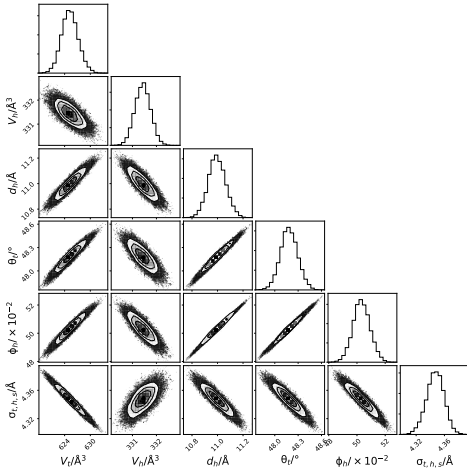


Figure S8: The multi-parameter PDFs for the chemically-relevant model of DLPC X-ray reflectometry data at 35 mNm^{-1} . Source: Datasets, figure files and running/plotting scripts are available under CC-BY.¹⁷

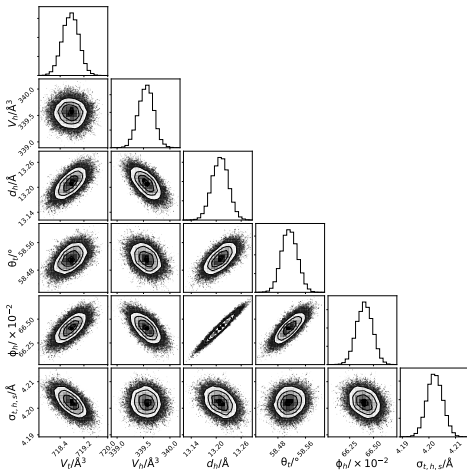


Figure S9: The multi-parameter PDFs for the chemically-relevant model of DMPC X-ray reflectometry data at 20 mNm^{-1} . Source: Datasets, figure files and running/plotting scripts are available under CC-BY.¹⁷

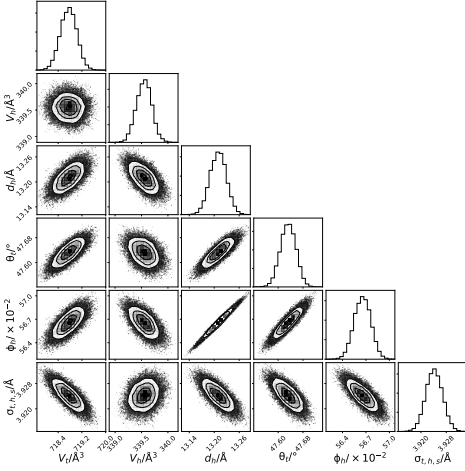


Figure S10: The multi-parameter PDFs for the chemically-relevant model of DMPC X-ray reflectometry data at 25 mNm^{-1} . Source: Datasets, figure files and running/plotting scripts are available under CC-BY.¹⁷

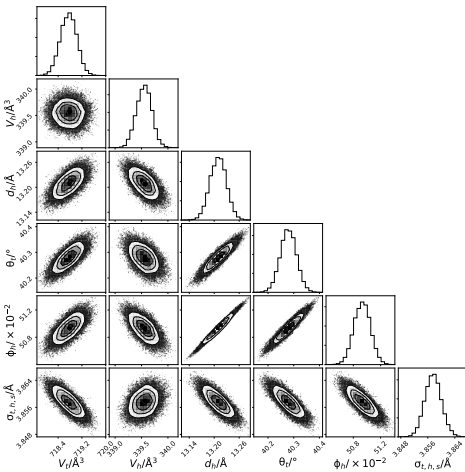


Figure S11: The multi-parameter PDFs for the chemically-relevant model of DMPC X-ray reflectometry data at 30 mNm^{-1} . Source: Datasets, figure files and running/plotting scripts are available under CC-BY.¹⁷

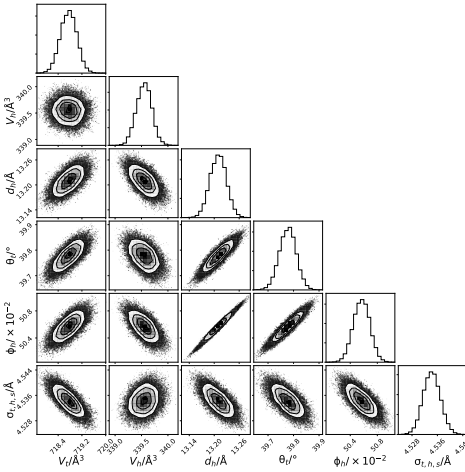


Figure S12: The multi-parameter PDFs for the chemically-relevant model of DMPC X-ray reflectometry data at 40 mNm^{-1} . Source: Datasets, figure files and running/plotting scripts are available under CC-BY.¹⁷

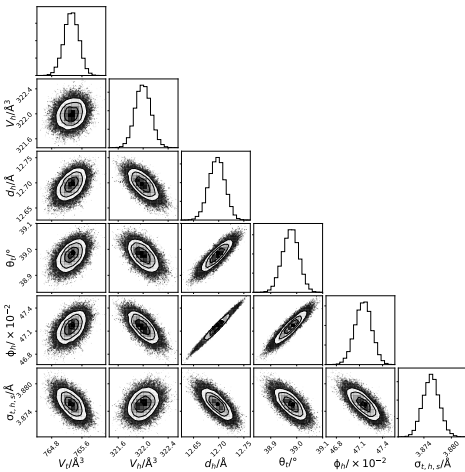


Figure S13: The multi-parameter PDFs for the chemically-relevant model of DPPC X-ray reflectometry data at 15 mNm^{-1} . Source: Datasets, figure files and running/plotting scripts are available under CC-BY.¹⁷

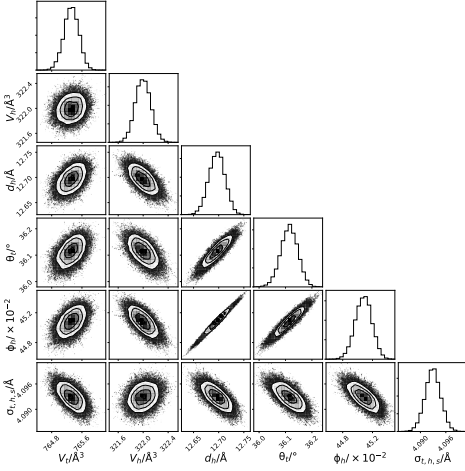


Figure S14: The multi-parameter PDFs for the chemically-relevant model of DPPC X-ray reflectometry data at 20 mNm^{-1} . Source: Datasets, figure files and running/plotting scripts are available under CC-BY.¹⁷

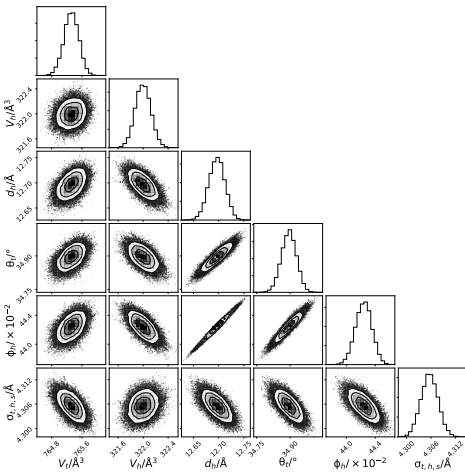


Figure S15: The multi-parameter PDFs for the chemically-relevant model of DPPC X-ray reflectometry data at 25 mNm^{-1} . Source: Datasets, figure files and running/plotting scripts are available under CC-BY.¹⁷

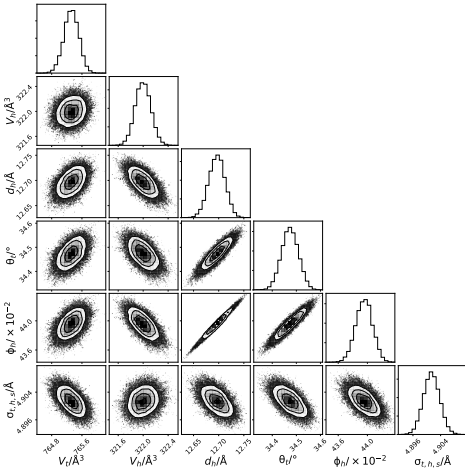


Figure S16: The multi-parameter PDFs for the chemically-relevant model of DPPC X-ray reflectometry data at 30 mNm^{-1} . Source: Datasets, figure files and running/plotting scripts are available under CC-BY.¹⁷

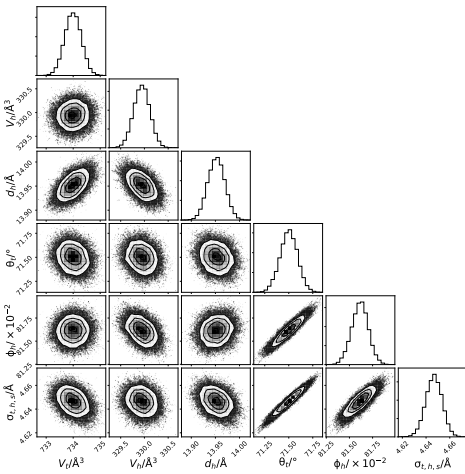


Figure S17: The multi-parameter PDFs for the chemically-relevant model of DMPG X-ray reflectometry data at 15 mNm^{-1} . Source: Datasets, figure files and running/plotting scripts are available under CC-BY.¹⁷

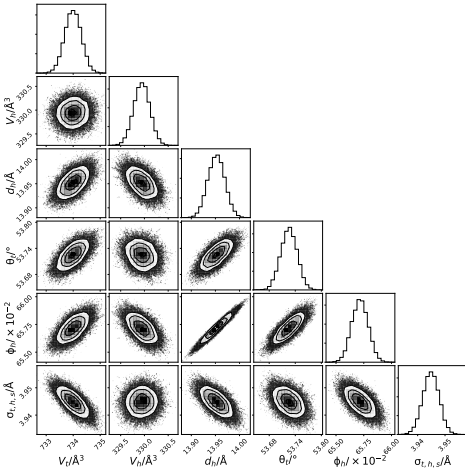


Figure S18: The multi-parameter PDFs for the chemically-relevant model of DMPG X-ray reflectometry data at 20 mNm^{-1} . Source: Datasets, figure files and running/plotting scripts are available under CC-BY.¹⁷

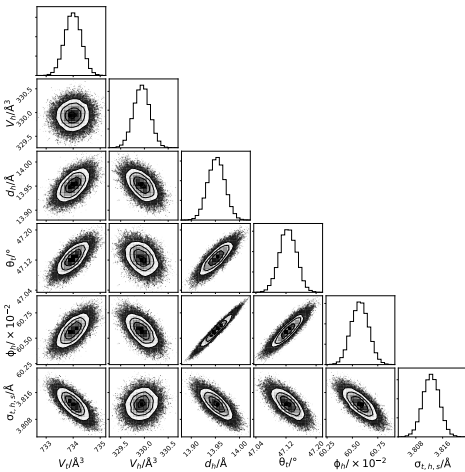


Figure S19: The multi-parameter PDFs for the chemically-relevant model of DMPG X-ray reflectometry data at 25 mNm^{-1} . Source: Datasets, figure files and running/plotting scripts are available under CC-BY.¹⁷

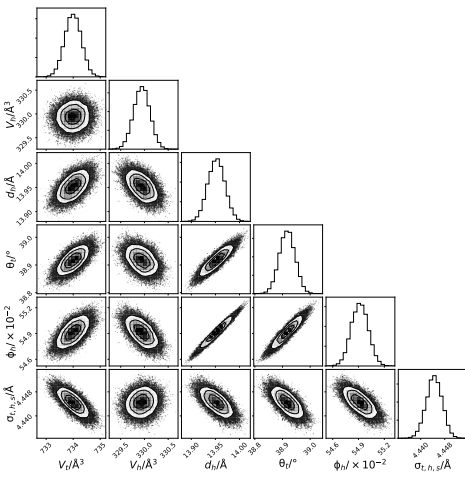


Figure S20: The multi-parameter PDFs for the chemically-relevant model of DMPG X-ray reflectometry data at 30 mNm^{-1} . Source: Datasets, figure files and running/plotting scripts are available under CC-BY.¹⁷

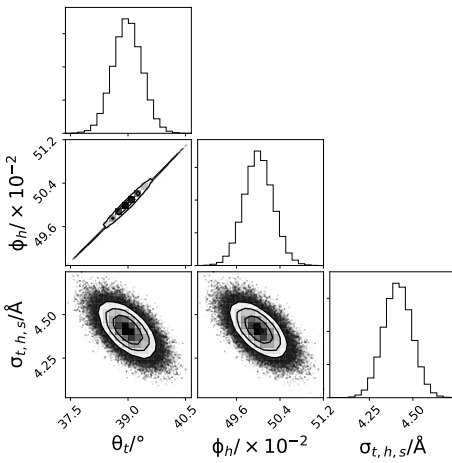


Figure S21: The multi-parameter PDFs for the chemically-relevant model of two contrast DMPC neutron reflectometry data at 20 mNm^{-1} . Source: Datasets, figure files and running/plotting scripts are available under CC-BY.¹⁷

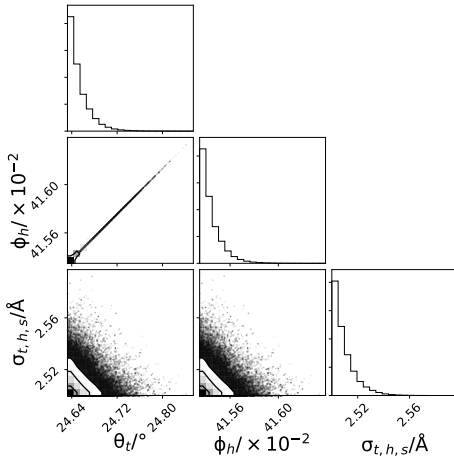


Figure S22: The multi-parameter PDFs for the chemically-relevant model of two contrast DMPC neutron reflectometry data at 25 mNm⁻¹. Source: Datasets, figure files and running/plotting scripts are available under CC-BY.¹⁷

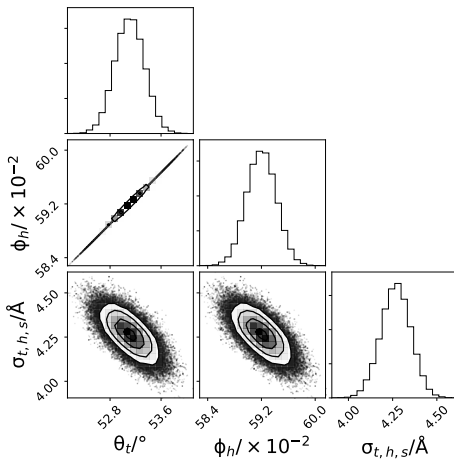


Figure S23: The multi-parameter PDFs for the chemically-relevant model of two contrast DPPC neutron reflectometry data at 15 mNm⁻¹. Source: Datasets, figure files and running/plotting scripts are available under CC-BY.¹⁷

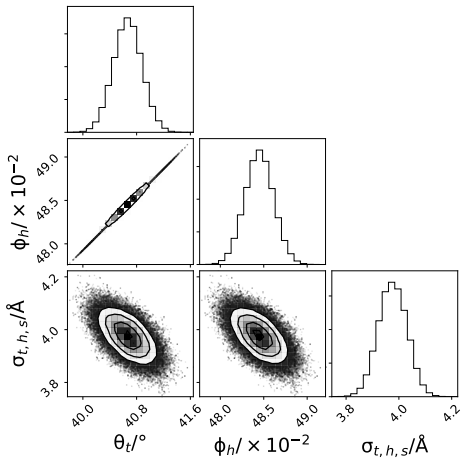


Figure S24: The multi-parameter PDFs for the chemically-relevant model of two contrast DMPC neutron reflectometry data at 20 mNm⁻¹. Source: Datasets, figure files and running/plotting scripts are available under CC-BY.¹⁷